Available online at www.sciencedirect.com

ScienceDirect

Underground Space 25 (2025) 176–194

www.keaipublishing.com/undsp

Research Paper

Effect of strain rate on the fracture behavior of granite under unconfined compression: A meso-scale energy evolution perspective

Qinyuan Liang [a], Hengxing Lan [a,b,*], Yu Zhou [c,f], Shijie Liu [a], Bo Li [d], Langping Li [b], Han Bao [e]

[a] College of Geological Engineering and Geomatics, Chang'an University, Xi'an 710054, China
[b] State Key Laboratory of Resources and Environmental Information System, Institute of Geographic Sciences and Natural Resources Research, Chinese Academy of Sciences, Beijing 100101, China
[c] Key Laboratory of Rock Mechanics and Geohazards of Zhejiang Province, Shaoxing University, Shaoxing 312000, China
[d] College of Civil Engineering, Tongji University, Shanghai 200092, China
[e] School of Highway, Chang' an University, Xi' an, Shaanxi 710064, China
[f] School of Geoscience and Technology, Southwest Petroleum University, Chengdu 610500, China

Received 27 October 2024; received in revised form 9 April 2025; accepted 31 May 2025
Available online 26 September 2025

Abstract

The macro mechanical behavior of rock material is attributed to the meso/mineral characteristics. To deeply reveal the mechanisms of strain rate effect on mechanical properties and crack propagation, a series of unconfined compression experiments and simulations for exploring the meso-scale characteristic were conducted at different strain rates. Based on the micro-loading equipment with microphotography capabilities and the numerical grain-based model method, the meso-scale crack propagation and energy evolution characteristics of granite during the pre-peak loading process were analyzed. The results indicate that with the increase of strain rate, the crack distribution entropy value increases, which means that cracks are more evenly distributed among various minerals. The differences in stored elastic strain energy among different minerals decrease, resulting in more uniform energy release. In addition, cracks associated with biotite transits from intergranular to transgranular modes. Therefore, the increased strain rate can prompt more minerals to participate in deformation, thereby enhancing the mechanical properties. This study deeply reveals the mechanisms of strain rate on granite crack propagation at the meso-scale, offering valuable insights for the stability and safety of underground space engineering.

Keywords: Granite; Strain rate effect mechanisms; Meso-scale; Crack propagation; Energy evolution

1 Introduction

Excavation operation in the underground space significantly influences the stress distribution and damage evolution of surrounding rock (Martin, 1993; Bao et al., 2020; Liang et al., 2022; He et al., 2023). Thus, a suitable excavation rate, which is highly related to the quasi-static strain rate effect, is essential to be determined first to ensure the safety of underground space engineering (Li et al., 2021; Xu et al., 2023; Xiao et al., 2023; Liu et al., 2024).

Studies indicate that increasing strain rates result in higher rock strength, greater elastic modulus, and faster crack propagation (Xie et al., 2020; Xiao et al., 2023). Furthermore, with higher strain rates, the energy released due to damage intensifies, reflected in more pronounced brittle failure characteristics (Gao et al., 2015). This implies that the energy evolution process is influenced by strain rate and plays a critical role in understanding rock failure mechanisms (Xie et al., 2009). Thus, over the past two decades, numerous studies have investigated rock behavior at

* Corresponding author at: College of Geological Engineering and Geomatics, Chang'an University, Xi'an 710054, China.
E-mail address: lanhx@igsnrr.ac.cn (H. Lan).
Peer review under the responsibility of Tongji University

https://doi.org/10.1016/j.undsp.2025.05.009

varying strain rates from an energy perspective (Liang et al., 2015; Li et al., 2021; Xu et al., 2023).

Variations in strain rate significantly influence the distribution and dissipation of energy within rocks, thereby altering crack propagation patterns (Liang et al., 2015). Li et al. (2014) conducted unconfined compression tests on coarse-grained marble and found that higher strain rates increase stored elastic energy, promoting brittle failure through tensile cracking. Similarly, Zhao et al. (2020) studied brittle granite under various loading rates, finding that higher rates significantly increased both total and elastic strain energy, leading to a sharper energy release during failure. This results in more severe rock bursts, particularly at higher strain rates. Additionally, Zhou et al. (2018) investigated the effect of loading rates on crack propagation speed and fracture toughness, showing that higher loading rates result in faster crack propagation due to the rapid accumulation and release of energy at the crack tip. Given that macro failure results from the extension, merging, and linking of micro-cracks, some researchers have explored this problem on a smaller scale. They found that energy accumulates more rapidly at higher strain rates, causing cracks to propagate from intergranular to transgranular fractures (Xu et al., 2023). Numerical studies using the grain-based model (GBM) by Li et al. (2018) replicated this phenomenon and demonstrated that transgranular cracks are associated with energy dissipation, while intergranular cracks relate to stress concentration between grains. They further demonstrated that cracking behavior strongly depends on the interface energy release rate (Li et al., 2021). These studies highlight the importance of examining rock material at the meso-scale. In summary, macroscopic failure and engineering instability are closely related to the propagation of microcracks (Feng et al., 2020, 2023; Xiao et al., 2024). The mechanical properties of different minerals significantly influence the initiation and propagation of cracks at varying strain rates, which, in turn, affect the stability of rock masses and the overall performance of underground engineering structures. However, detailed knowledge regarding the behavior of different minerals (such as quartz, feldspar, and biotite) and the evolution of energy under different strain rates remains lacking. Furthermore, due to limitations in experimental equipment, the dynamic progressive crack processes at the meso-scale, which are crucial for validating numerical results, have yet to be captured.

To address these limitations, this study utilized an in-situ micro-mechanical tester, equipped with a real-time optical microscope, to capture crack propagation at the meso-scale. GBM-based numerical simulations were performed to provide detailed insights into how different minerals store and release energy under varying strain rates. By integrating experimental observations with numerical modeling, this research seeks to uncover the microscopic mechanisms by which increased strain rates influence energy dynamics and improve the mechanical properties of rocks. Ultimately, this study provides important implications for the design and stability assessment of underground space engineering.

2 Experimental and numerical simulation methods

2.1 Sample preparation

The granite samples used in this study were obtained from Jining, Shandong Province, with grain sizes ranging from 0.1 to 0.5 mm. X-ray diffraction (XRD) analysis revealed that the primary rock-forming minerals are plagioclase (34.9%), quartz (27.4%), microcline (22.7%), biotite (12.5%), and kaolinite (2.5%). To enable real-time observation of crack propagation during testing, the samples were prepared into rectangular prisms measuring 8 mm × 8 mm × 16 mm, as shown in Fig. 1(a).

2.2 Equipment and test scheme

The experimental setup was adapted from a miniature mechanical device miniature tensile instrument-light microscope (MTI-LM), comprising a Fullam SEM 2000 tensile tester and an optical microscope, as shown in Fig. 1(b). This system provides high precision, automatic servo control, and real-time data acquisition, making it suitable for a wide range of applications, including bending tests (Rinehart et al., 2015), unconfined compression tests (Huang et al., 2020), and tensile tests (Liu et al., 2022).

Following previous studies (Xiao et al., 2023), three sets of loading rate tests were conducted at 0.001, 0.010, and 0.100 mm/s. The corresponding strain rates were 6.25×10^{-5}, 6.25×10^{-4}, and 6.25×10^{-3} s^{-1}, respectively,

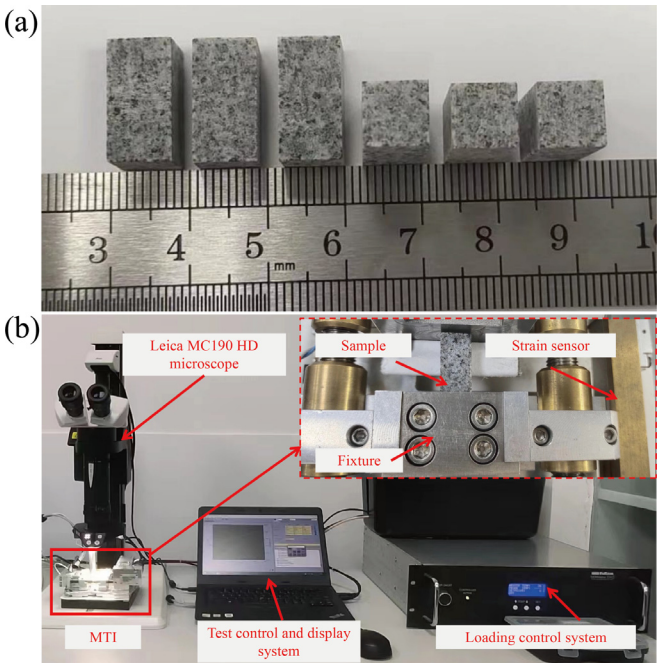

Fig. 1. Granite specimen and experimental setup. (a) Granite specimen, and (b) loading apparatus.

Table 1
Size of prepared samples and test scheme.

Sample number	Length (mm)	Width (mm)	Height (mm)	Loading rate (mm/s)	Strain rate (s^{-1})
G1-1	8.01	7.99	16.03	0.001	6.25×10^{-5}
G1-2	8.02	8.00	16.12		
G1-3	8.04	8.05	15.96		
G2-1	7.95	7.90	15.99	0.010	6.25×10^{-4}
G2-2	8.08	8.05	15.98		
G2-3	8.01	8.00	16.04		
G3-1	7.90	7.88	15.95	0.100	6.25×10^{-3}
G3-2	8.02	7.99	15.98		
G3-3	7.92	7.90	15.94		

all within the quasi-static strain rate range (Xie et al., 2020). The detailed test scheme is provided in Table 1. The imaging scheme involved capturing individual photos before and after loading, with the entire process monitored in real-time via a microscope. Recording was performed at 25 frames per second to capture the progression during testing.

2.3 GBM establishment and microscopic parameter calibration

The GBM method is advantageous as it enables the differentiated assignment of properties to individual mineral grains, accurately replicating the heterogeneous nature of mineral crystals within the rock (Potyondy & Cundall, 2004; Lan et al., 2010, 2013; Peng et al., 2018; Zhou et al., 2024a, 2024b). This allows the model to more precisely capture the effects of strain rate on energy evolution within distinct mineral structures.

The GBM model employed in this study is based on PFC2D, and the modeling process is as follows:

(1) An initial sample was generated with large particles in accordance with the mineral content and particle sizes outlined in Section 2.1 (Fig. 2(a));
(2) Voronoi cells were created using the Qhull program (Barber et al., 1996), with the centroid of each cell positioned at the center of each large particle (Fig. 2(b));
(3) Smaller particles were filled within each Voronoi polygonal region to simulate fracturable minerals (Fig. 2(c));
(4) Contact models were assigned (Fig. 2(d)). The contact model within the mineral grains was the parallel-bonded model (PBM), while the model between grains was the smooth-joint model (SJM), as illustrated in Fig. 2(e), with their corresponding movement modes shown in Fig. 2(f) (Lambert & Coll, 2014; Zhou et al., 2024a).

The parameter calibration is based on the laboratory results from the unconfined compression and Brazilian tests, as shown in Table 2. Figure 3 illustrates the numerical simulation tests used for this calibration. The basic

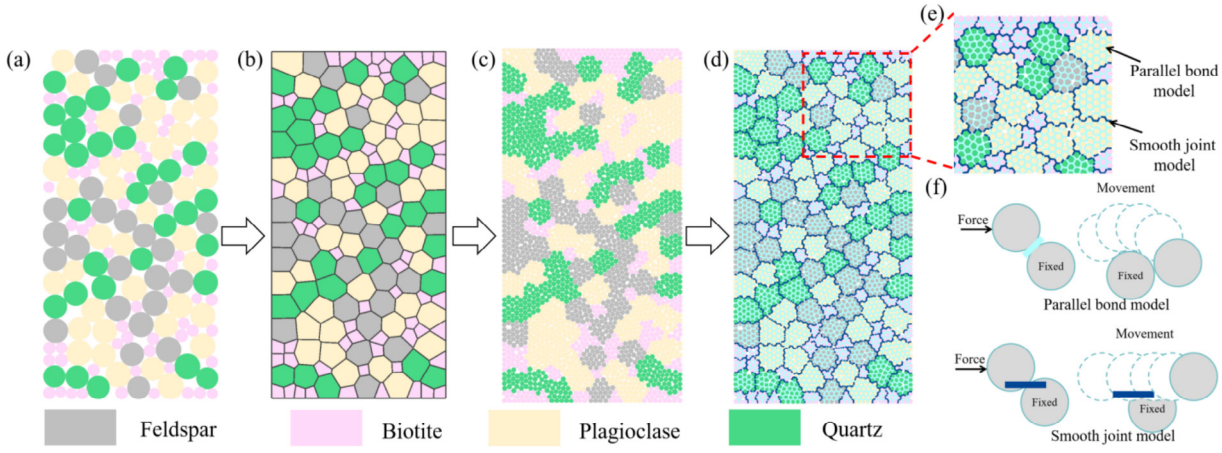

Fig. 2. Schematic representation of the GBM model establishment. (a) Initial sample composed of large particles, (b) Voronoi polygonal division of the sample, (c) smaller particles filled within the Voronoi polygon regions, (d) assignment of intragranular and intergranular contact models, (e) characteristics of the PBM and SJM, and (f) movement modes of PBM and SJM.

Table 2
Macro-mechanical properties as obtained from laboratory tests and simulations.

Macro-mechanical properties	Laboratory average value	Numerical average value	Error (%)
UCS (MPa)	12.10	12.57	3.88
Elastic modulus (GPa)	30.65	30.28	1.21
Brazilian tensile strength (MPa)	1.92	2.05	6.77
Tensile modulus (GPa)	14.83	14.28	3.71

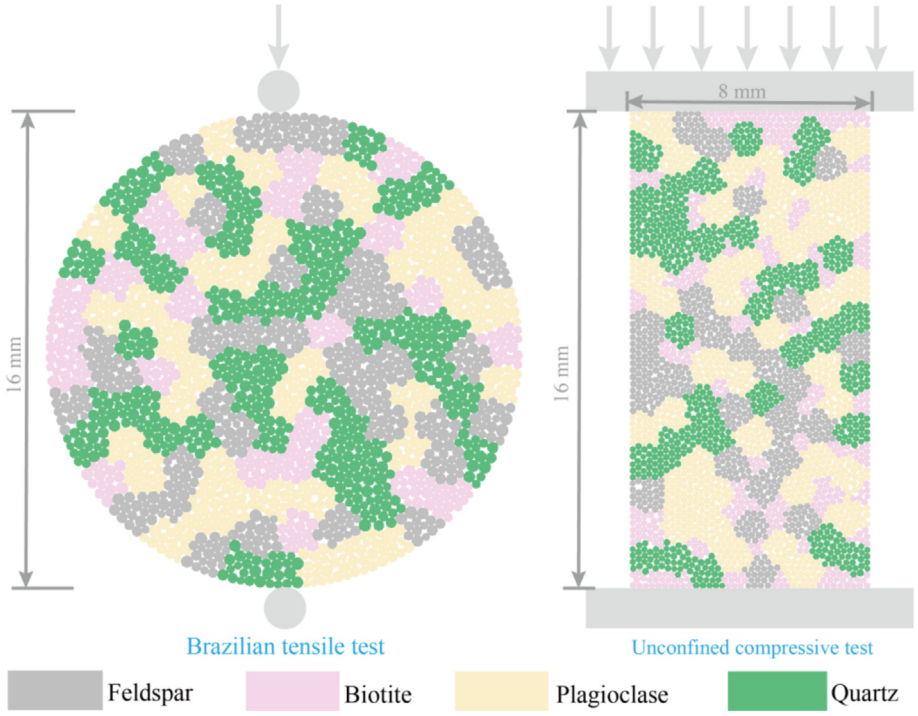

Fig. 3. Schematic of the GBM model specimen for parameter calibration.

guidance for calibration is the general mineral microscopic mechanical properties, including effective modulus, tensile strength, and compressive strength, with the sequence of: quartz > plagioclase and potassium feldspar > biotite > mineral interface (Lan et al., 2010, 2013; Peng et al., 2018; Zhou et al., 2024a). Prior to conducting parameter calibration, the following fundamental modeling assumptions were also defined: (1) Constitutive parameters associated with intra-mineral contacts within each mineral were specified as fixed values. (2) The friction coefficient between specimen ends and loading platens was set to zero to eliminate boundary constraint effects.

The sample size and loading rate were kept consistent with the experimental conditions. The microscopic parameter calibration procedure followed the method proposed by Potyondy and Cundall (2004), Saadat and Taheri (2019a, 2019b), and Zhou et al. (2025), as follows:

(1) Particle property assignment. The particle size and mineral density were assigned based on previous studies (Peng et al., 2018; Liang et al., 2025b).
(2) Elastic modulus and tensile modulus calibration. The macro elastic modulus and tensile modulus were calibrated by adjusting the PBM modulus, PBM normal-to-shear stiffness ratio, mineral intergranular SJM contact normal stiffness factor, and SJM shear normal stiffness factor for each mineral.
(3) Macro tensile strength calibration. The macro tensile strength obtained from the Brazilian test was calibrated by adjusting the PB tensile strength within the mineral grains and the SJ bond tensile strength between grains. Additionally, the friction parameters (friction angle and friction coefficient) within and between grains were adjusted to match the numerical simulation results with the experimental results.
(4) Unconfined compressive strength (UCS) calibration. The UCS was calibrated by adjusting the PBM cohesion within the mineral grains and the SJ bond cohesion strength between grains.

Since multiple microscopic parameters can influence various macro parameters, these steps typically require

multiple iterations to achieve satisfactory calibration results. The parameters calibrated based on these steps are shown in Table 3. The macro-mechanical properties from the simulation results and laboratory tests are listed in Table 2, and error analysis shows that the numerical results closely match the experimental results. Using these calibrated parameters, numerical tests for unconfined compression at different strain rates were conducted.

To ensure result accuracy, three random seeds were used to generate samples with different mineral distributions, labeled GBM1, GBM2, and GBM3.

2.4 Principle of energy calculation

Under unconfined compression, the rock specimen system maintains dynamic energy equilibrium with the external environment, and the internal energy evolution obeys the law of energy conservation (Xie et al., 2009, 2020; Cho, 2013). To investigate the failure behavior of granite and the energy evolution of constituent minerals under different strain rates, a customized energy calculation program was developed. The analysis particularly focuses on the pre-peak stage, during which energy accumulation and microcrack initiation play dominant roles.

Given the small size of the specimen, gravitational potential energy is negligible. The total input energy of the system ΔU^{c}, provided by the unconfined compressive load, is assumed to be entirely converted into elastic strain energy ΔU^{e}, dissipated energy ΔU^{d}, and kinetic energy ΔU^{k}. The energy conservation equation is thus simplified as (Tu et al., 2016; Zhou et al., 2023):

$$\Delta U^{c} = \Delta U^{e} + \Delta U^{d} + \Delta U^{k}. \tag{1}$$

Elastic strain energy characterizes the ability of materials to absorb and store energy under stress, which is essential for evaluating crack initiation and propagation (Zhou et al., 2023). Therefore, only the elastic strain energy is considered in the current analysis. The elastic strain energy is obtained using the following equation:

$$\Delta U^{e} = \sum\nolimits_{i=1}^{n} u_{t,i}^{e} - \sum\nolimits_{i=1}^{n} u_{0,i}^{e}, \tag{2}$$

where n is the total number of particles in the system, and $u_{0,i}^{e}$ and $u_{t,i}^{e}$ are the elastic energy densities of the i-th particle at the initial state and at time t, respectively.

To further analyze the contribution of individual mineral phases, the total elastic strain energy is decomposed into four components corresponding to quartz, feldspar, plagioclase, and biotite:

$$\Delta U^{e} = \Delta U^{e\_Quartz} + \Delta U^{e\_Feldspar} + \Delta U^{e\_Plagioclase} + \Delta U^{e\_Biotite}. \tag{3}$$

The elastic energy associated with each mineral phase is calculated using the following formulation:

Table 3
Microscopic parameters of the GBM model.

	Microparameters	K-feldspar	Quartz	Plagioclase	Biotite
Microproperties of the particle	Minimum particle radius, R_{min} (mm)	0.15	0.15	0.15	0.15
	Particle/size ratio, R_{max}/R_{min}	1.66	1.66	1.66	1.66
	Particle density, ρ (kg•m^{-3})	2600	2650	2600	2850
Microproperties of the mineral contacts (PBM)	PB modulus, pb_emod (GPa)	7	9	7	6
	PB normal-to-shear stiffness ratio, pb_krat	1.6	1.0	1.7	1.1
	PB cohesion, pb_coh (MPa)	27.5	28.5	27.5	23.0
	PB tensile strength, pb_ten (MPa)	3.1	3.5	3.1	2.0
	PB friction angle, pb_fa (°)	20	20	20	20
	PB friction coefficient, pb_fric	1.0	1.0	1.0	1.0
Microproperties of the mineral boundaries (SJM)	SJ bond cohesion strength, sj_coh (MPa)	16			
	SJ bond tensile strength,sj_ten (MPa)	4			
	SJ bond friction angle, sj_fa (°)	20			
	SJ bond friction coefficient, sj_fric	0.3			
	SJ contact normal stiffness factor	0.9			
	SJ shear normal stiffness factor	0.3			

$$\Delta U^{e\text{-}M} = \sum_{i=1}^{n\text{-}M} u_{t,i}^{e} - \sum_{i=1}^{n\text{-}M} u_{0,i}^{e}, \quad M \in \{\text{Quartz, Feldspar, Plagioclase, Biotite}\}. \tag{4}$$

For each particle, the elastic energy density is calculated based on its stress state and volume:

$$u_i^{e} = \frac{V_i}{2E_0}\left[\sigma_1{}^2 + \sigma_3{}^2 - 2\mu\sigma_1\sigma_3\right], \tag{5}$$

where V_i is the volume of the i-th particle, E_0 is the initial elastic modulus, μ is Poisson's ratio (approximately 0.25), and σ_1, σ_3 are the major and minor principal stresses, respectively.

3 Results analysis

3.1 Effect of strain rate on mechanical properties

To capture the entire failure process, stress–strain curves for granite samples at different strain rates were plotted, as shown in Fig. 4(a), (b), and (c). Based on these stress–strain curves, the process can be divided into three stages: compaction of pores and fissures (Region I), elastic deformation to stable microcrack development (Region II), and unstable fracture phase (Region III). Specifically, during the initial loading phase, as the load increases, the pre-existing micropores in the sample gradually close, leading to rock compaction and forming early nonlinear deformation. At this stage, the stress–strain curve exhibits a concave downward shape, referred to as the crack closure stage of pores and fissures (Region I). Following this stage, the stress–strain curve becomes nearly linear, indicating stable microcrack propagation (Region II), which shortens progressively with increasing strain rate. After the elastic phase, the miniature tensile instrument (MTI) system is used to directly observe crack propagation, as the sample transitions from volumetric compression to dilation until peak strength is reached, representing the unstable fracture stage (Region III). It is important to note that this study focuses only on the pre-peak stage, as this stage is crucial for understanding the initiation and development of cracks, which play a significant role in the crack behavior of the material (Eberhardt et al., 1999). Figure 4(d) shows the evolution of strength with strain rate. It is evident that as the strain rate increases, the strength of granite also increases. When the strain rate increases from 6.25×10^{-5} to 6.25×10^{-3} s^{-1}, the average peak strength increases from 12.10 to 14.37 MPa, representing an increase of 18.76.

To obtain the influence of strain rate on the elastic modulus of granite, the average elastic modulus of the rock was calculated using Eq. (6). Here, E_{av} represents the average elastic modulus of the rock (GPa); σ_a represents the stress corresponding to the start point of the axial strain curve's linear segment (MPa) (red dots shown in Fig. 4); σ_b represents the stress corresponding to the endpoint of the axial strain curve's linear segment (MPa) (green dots shown in Fig. 4); ε_{lb} represents the axial strain at stress σ_b; ε_{la} represents the axial strain at stress σ_a. The resulting evolution curve of the elastic modulus with strain rate is shown in Fig. 4(e). As the strain rate increases, the elastic modulus of the rock also increases. When the strain rate changes from 6.25×10^{-5} to 6.25×10^{-3} s^{-1}, the average elastic modulus increases from 30.65 to 35.90 GPa, representing an increase of 17.13%.

$$E_{av} = \frac{\sigma_b - \sigma_a}{\varepsilon_{lb} - \varepsilon_{la}}. \tag{6}$$

To better analyze the effect of strain rate on the deformation behavior of granite, the axial strain corresponding to the peak strength was recorded, as shown in Fig. 4(f). As the strain rate increases, the axial strain also exhibits an increasing trend. When the strain rate increases from 6.25×10^{-5} s^{-1} to 6.25×10^{-3} s^{-1}, the average axial strain rises from 0.067% to 0.084%, representing a 25.37% increase.

Figure 5 presents the numerical simulation results at different strain rates. Figure 5(a) and (b) shows the peak strength and elastic modulus of the GBM model at different rates, respectively. The results indicate that both the peak strength and elastic modulus of the GBM model increase with increasing strain rates. Specifically, when the strain rate increases from 6.25×10^{-5} to 6.25×10^{-3} s^{-1}, the average peak strength of the GBM model increases from 12.57 to 14.74 MPa, an increase of 17.26%; and the average elastic modulus increases from 30.28 to 34.98 GPa, an increase of 15.52%. When comparing the increase in peak strength and elastic modulus from the experiments, the GBM model results closely match the experimental data, indicating that the strain rate response pattern of the GBM model is consistent with actual behavior.

The rock failure process involves crack initiation, development, and coalescence (Bao et al., 2021; Liang et al., 2025a, 2025c), making it essential to obtain the characteristic stress points. The method for identifying these points follows the procedure previously described. To better compare the contribution of each characteristic stress to the failure process, the crack initiation stress (σ_{ci}) and crack damage stresses (σ_{cd}) were normalized against the peak stress (σ_p) (as shown in Fig. 6). It can be observed that as the strain rate increases, the peak strength (σ_p) gradually increases, while the crack initiation stress (σ_{ci}) and damage stress (σ_{cd}) remain relatively stable. The normalized values of σ_{ci}/σ_p and σ_{cd}/σ_p gradually decrease. Specifically, with increasing strain rate, the normalized σ_{ci}/σ_p decreases from 0.43 to 0.37, a reduction of 13.95%, and the normalized σ_{cd}/σ_p decreases from 0.82 to 0.71, a reduction of 13.41%. These trends are consistent with the results of previous studies (Wang et al., 2011; Zhu et al., 2020; Yu et al., 2023).

3.2 Effect of strain rate on failure modes

To further explore the impact of strain rates on failure modes, Fig. 7 illustrates the unconfined compression failure

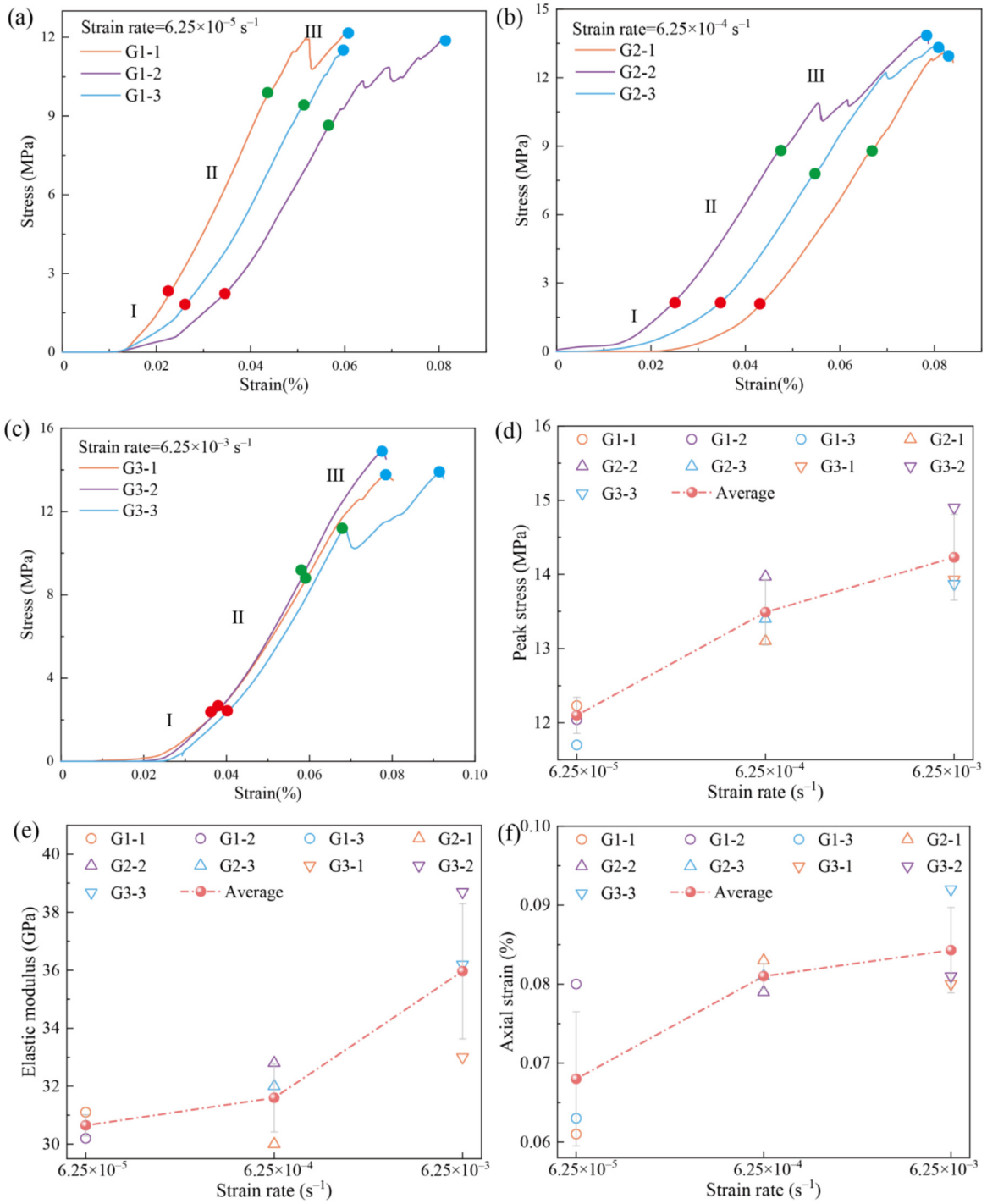

Fig. 4. Strain rate test results. (a), (b), and (c) show the stress–strain curves of rocks at strain rates of 6.25×10^{-5}, 6.25×10^{-4}, and 6.25×10^{-3} s^{-1}, respectively, (d) evolution of strength with strain rate, (e) evolution of elastic modulus with strain rate, and (f) evolution of axial strain with strain rate.

patterns of the samples at different strain rates. The results show that at lower strain rates, the samples tend to fracture into large blocks, while at higher strain rates, the failure is predominantly characterized by pulverization. These findings are consistent with those reported in previous studies (Doan & Gary, 2009; Li et al., 2014). Combined with the results from Fig. 4, it can be observed that as the strain rate increases, the strength, elastic modulus, and axial strain of granite exhibit greater variability. This may be due to the fact that at lower strain rates, internal crack propagation in the specimen is relatively stable, with micro-cracks converging along local weak planes, resulting in blocky fragmentation. However, as the strain rate increases, internal crack propagation within the specimen accelerates significantly and becomes more uniform, ultimately leading to a pulverized failure mode.

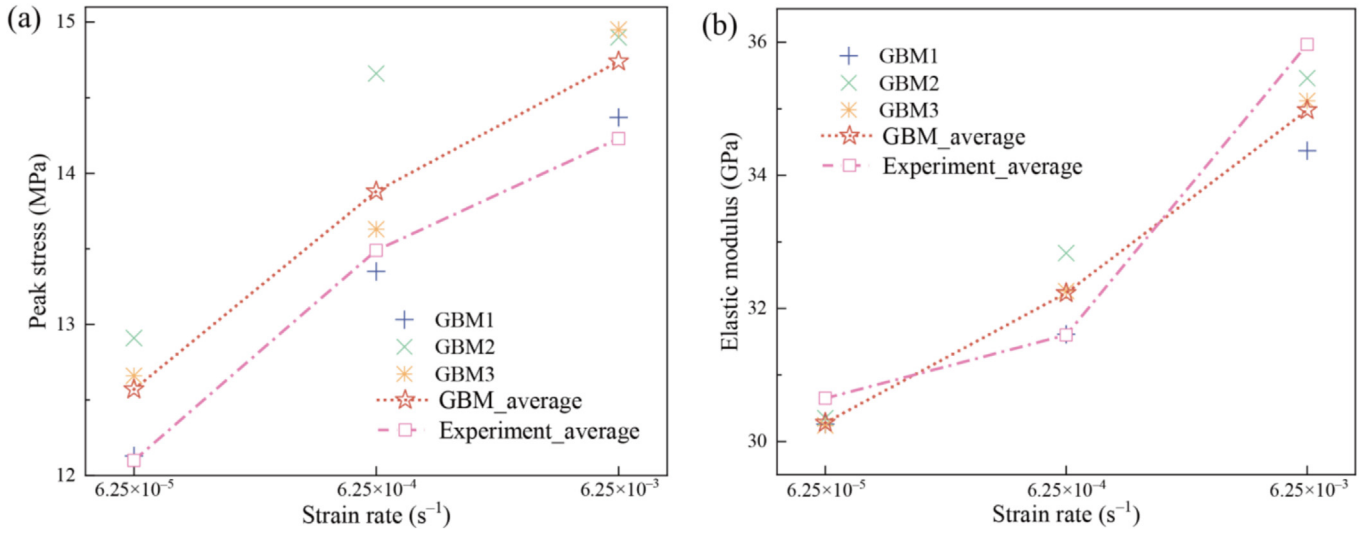

Fig. 5. GBM model results at different strain rates. (a) Peak strength results of the GBM model at different strain rates, and (b) elastic modulus results of the GBM model at different strain rates.

To further investigate the effect of strain rate on crack propagation at the meso-scale, the MTI-LM system was employed to observe the detailed failure process of granite under varying strain rates. The MTI-LM system enables direct observation of crack behavior, capturing images throughout the entire failure process (Liu et al., 2022). Figure 8 presents the microstructural failure of granite at strain rates of 6.25×10^{-5}, 6.25×10^{-4}, and 6.25×10^{-3} s^{-1}, with the specimens predominantly exhibiting splitting failure. Figure 8(c)–(e), (h)–(j), and (m)–(o) displays magnified views of specific stages within the white rectangular areas, corresponding to the beginning of the elastic region (Region I), the onset of unstable crack propagation (Region II), and the peak stress point (Region III) on the stress–strain curves in Fig. 4(a), (b), and (c). In Fig. 8, the white minerals are quartz, the gray minerals are feldspar, and the black minerals are biotite.

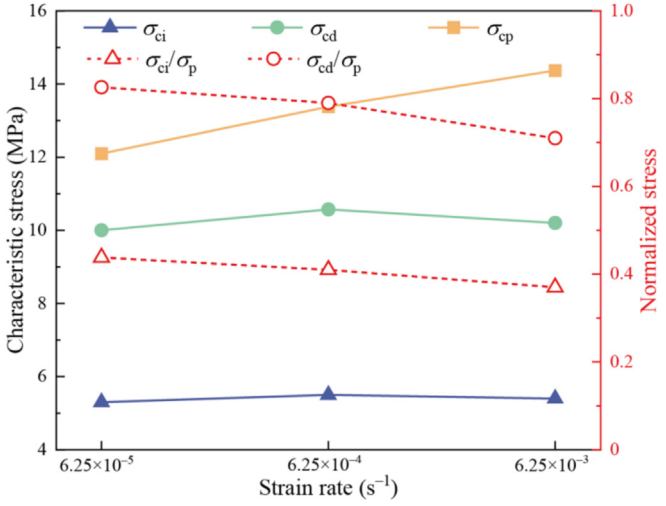

Fig. 6. Influence of strain rate on the characteristic stresses.

At a strain rate of 6.25×10^{-5} s^{-1}, as shown in Fig. 8(c), (d), and (e), a macro-crack nearly parallel to the loading direction is primarily observed, with cracks mainly propagating along mineral grain boundaries. This indicates that at low strain rates, the weak points at grain boundaries are more likely to serve as crack propagation paths. Additionally, when cracks propagate through biotite minerals, a noticeable intergranular phenomenon occurs, suggesting that biotite governs crack propagation. As the strain rate increases to 6.25×10^{-4} s^{-1}, the crack propagation path becomes more complex, though the controlling effect of biotite remains evident, as shown in Fig. 8(h), (i), and (j). There is an increase in both intragranular and intergranu-

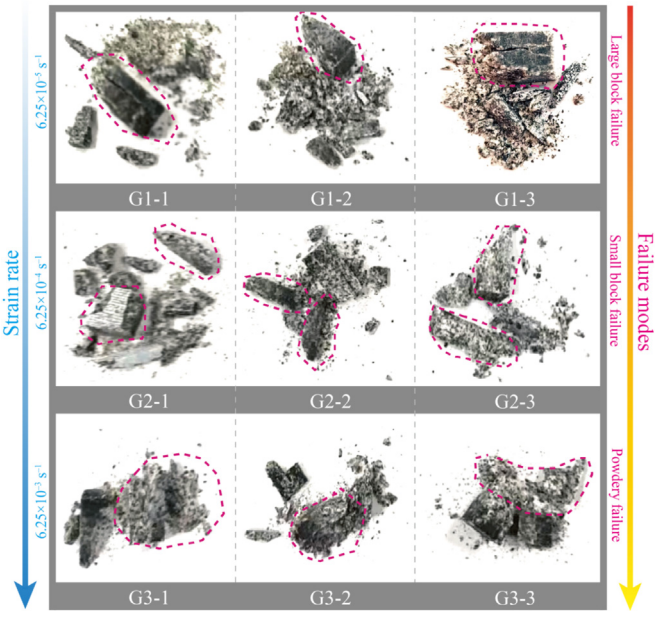

Fig. 7. Unconfined compression failure modes of specimens at different strain rates.

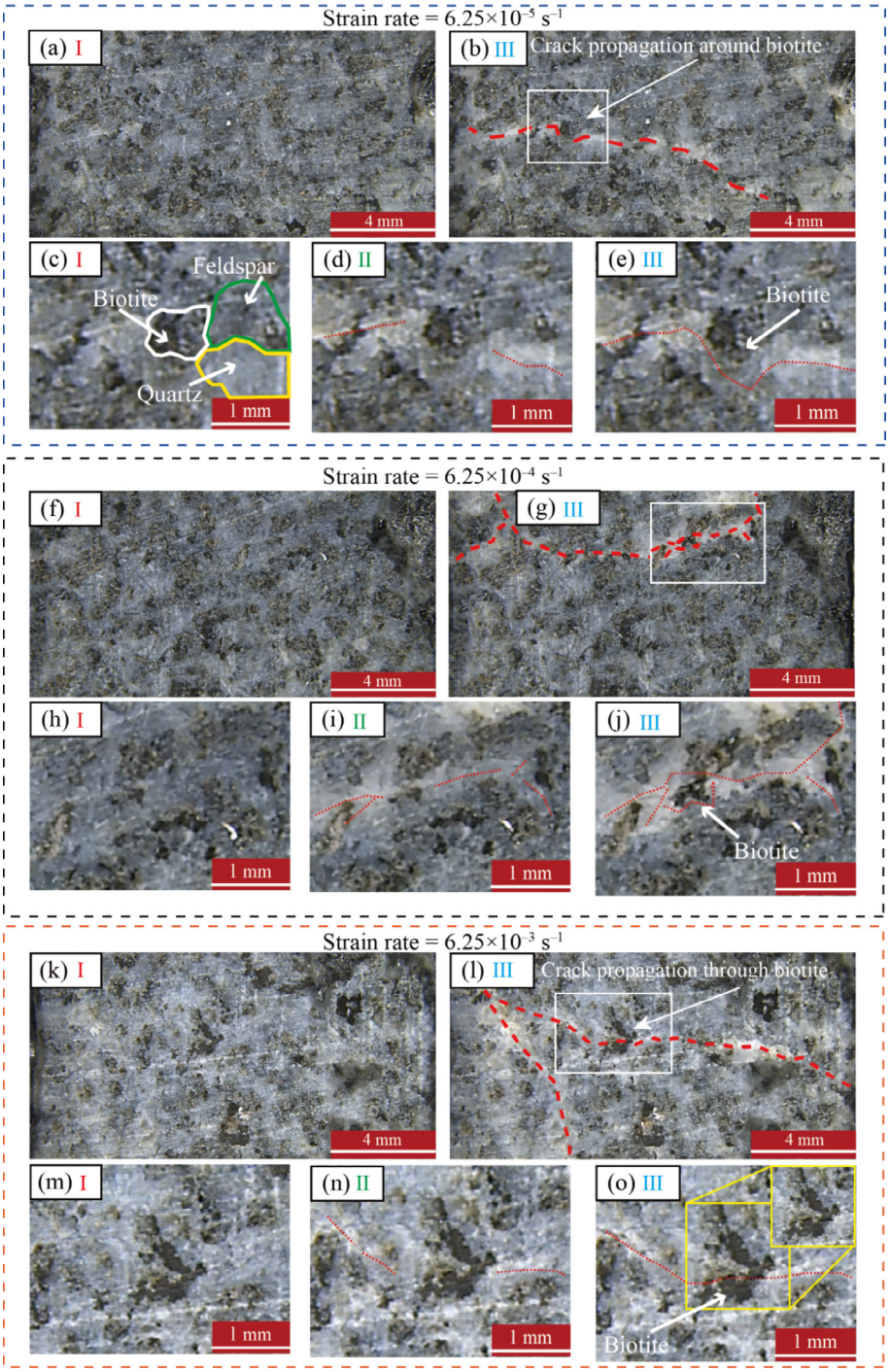

Fig. 8. Failure process of granite under different strain rates (Note: (a), (f), and (k) show images at the red points in Fig. 4; (b), (g), and (i) show images at the blue points (peak stress) in Fig. 4. The remaining images present magnified views of the white boxed regions at the red, green, and blue points (peak stress) for each strain rate).

lar crack propagation, especially within feldspar minerals. At a strain rate of 6.25×10^{-3} s^{-1} (Fig. 8(m), (n), and (o)), there is a significant increase in cracks within quartz and feldspar minerals. Cracks propagate directly through biotite, indicating that the controlling effect of biotite on crack propagation diminishes with increasing strain rate.

To more precisely investigate the effect of strain rate on the interaction between cracks and minerals, we performed thin section analysis of the fractured granite samples using polarized light microscopy, with the results shown in Fig. 9. At a strain rate of 6.25×10^{-5} s^{-1}, cracks predominantly propagated along mineral interfaces, especially between biotite and other minerals such as quartz and feldspar. The cracks tended to bypass biotite, propagating along the mineral interfaces, suggesting that biotite plays a role in limiting crack propagation through the mineral.

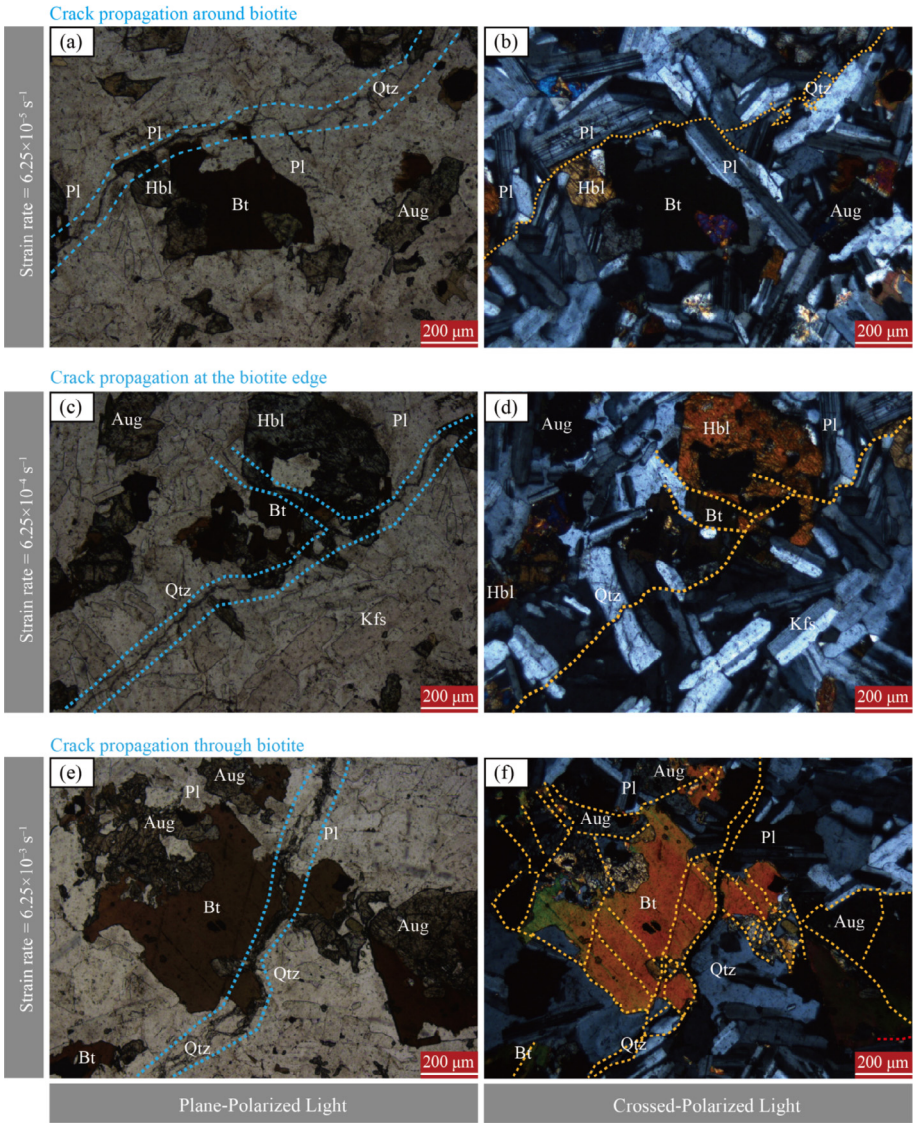

Fig. 9. Polarized microscopy of fractured specimens at different strain rates (Note: The blue dashed lines indicate the propagation of macroscopic cracks, while the orange-yellow dashed lines represent the propagation of microcracks. 'Bt' is short for biotite, 'Qtz' is short for quartz, 'Pl' is short for plagioclase, 'Kfs' is short for K-feldspar, 'Hbl' is short for hornblende, and 'Aug' is short for pyroxene).

As the strain rate increased to 6.25×10^{-4} s^{-1}, the crack propagation path became more complex, with cracks beginning to penetrate through the edges of biotite grains, indicating a reduction in biotite's ability to impede crack growth. At a strain rate of 6.25×10^{-3} s^{-1}, cracks directly penetrated biotite and extended into the interior of other minerals. The crack propagation was no longer significantly influenced by mineral interface structures, and the effect of biotite on crack propagation almost vanished, allowing the cracks to pass through biotite and continue propagating through other minerals.

In summary, from Fig. 9, it is evident that the influence of biotite on crack propagation decreases with increasing strain rate, with cracks transitioning from bypassing biotite to directly penetrating it. At low strain rates, biotite impedes crack growth, but this effect weakens as the strain rate increases.

4 Discussion

4.1 Evolution of microcracks at the meso-scale

To gain further insight into the evolution of microcracks under varying strain rates, the distribution of cracks at different loading stages was analyzed. Figure 10(a), (b), and (c) depicts the distribution of microcracks at different loading stages (σ_{ci}, σ_{cd}, and σ_p) under different strain rates. As the strain rate increases from 6.25×10^{-5} to 6.25×10^{-3} s^{-1}, significant changes occur in the distribution and types of cracks. At low strain rates, cracks are primarily intragranular tensile cracks and are relatively few in number. However, as the strain rate increases, the types of cracks become more complex, with a notable increase in intragranular shear cracks and intergranular cracks. The crack network also becomes more intricate and dense, especially in the

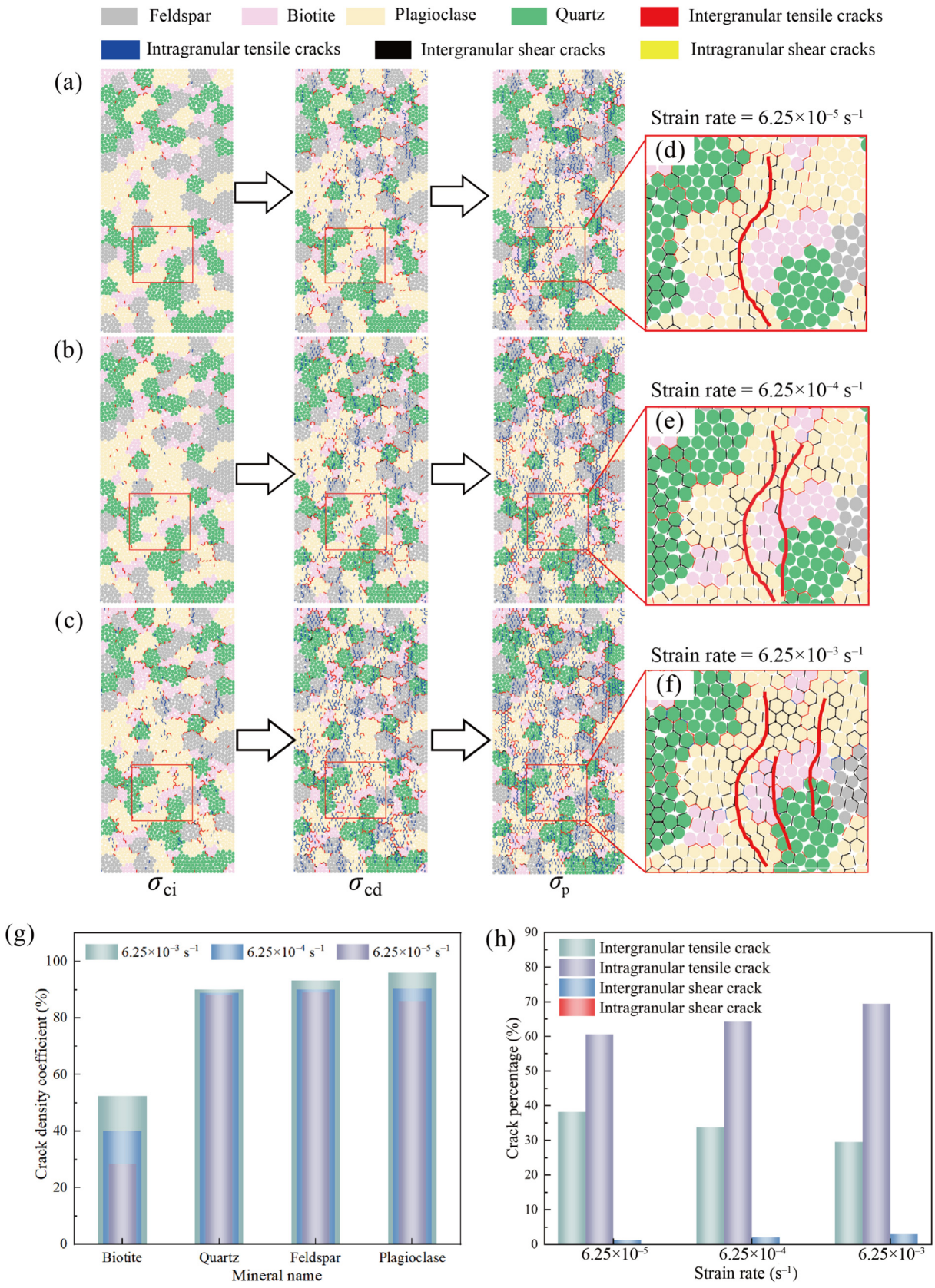

Fig. 10. Evolution of microcracks in the GBM model under varying strain rates. (a)–(c) show damage progression at strain rates of 6.25×10^{-5}, 6.25×10^{-4}, and 6.25×10^{-3} s^{-1}, respectively, (d)–(f) present magnified views of fractures involving biotite minerals at the same strain rates, (g) illustrates the microcrack coefficient in different minerals, and (h) displays the normalized percentage of microcrack types within the crystal structure.

areas near biotite (pink), where the concentration and density of cracks are highest. As strain rate increases, cracks transition from propagating around biotite to penetrating through it, which is consistent with the experimental results shown in Fig. 10(d), (e), and (f).

To quantitatively analyze the influence of different loading rates on the evolution of microcracks in minerals, the crack density coefficient defined by Li et al. (2022) was used. This coefficient quantitatively describes the number of microcracks originating within different minerals per unit area. A smaller coefficient indicates that cracks are less likely to originate, suggesting relatively minor damage, whereas a larger coefficient indicates greater damage. The formula for calculating this coefficient is as follows:

$$K_M = \frac{N_M}{C_M} \times 100\%, \quad M \in \{\text{Quartz, Feldspar, Plagioclase, Biotite}\}, \tag{7}$$

where K_M is the crack density coefficient, N_M represents the number of cracks inside the mineral, and C_M represents the mineral content.

Based on Eq. (7), the crack density coefficients under different strain rates were statistically analyzed at the failure point (Fig. 10(g)). It can be observed that at the same strain rate, the crack density coefficients per unit area for quartz, feldspar, and plagioclase are similar, whereas the crack density coefficient per unit area for biotite is significantly lower than that of other minerals. This indicates that quartz, feldspar, and plagioclase are more severely damaged, while biotite sustains less damage. With the increase in strain rate, the crack density coefficients K_M of all four minerals increase, ranked in descending order as: biotite > plagioclase > feldspar > quartz. Among them, the crack density coefficient per unit area for biotite increases significantly, from 28.0% to 52.4%, with an overall increase amplitude of 87.14%. Combined with Fig. 10(a), (b), and (c), it is evident that as the strain rate increases, the overall degree of damage in all four minerals intensifies, with biotite being the most prominent. The microcracks initially expand along the weak planes of biotite and eventually penetrate through it.

To further quantitatively compare the differences in microcrack initiation at different strain rates, the various types of cracks were normalized with respect to the total number of cracks (Fig. 10(h)). With the increase in strain rate, the normalized intergranular tensile cracks gradually decrease, the intragranular tensile cracks gradually increase, and the intergranular shear cracks remain nearly unchanged. Specifically, as the strain rate increases, the normalized intergranular tensile cracks decrease from 38.19% to 29.55%, a reduction of 22.62%, while the intragranular tensile cracks increase from 60.57% to 69.50%, an increase of 14.74%. These trends are consistent with the experimental results and previous studies (Li et al., 2020).

According to the results above, strain rate significantly affects the crack propagation and aggregation. To quantify the degree of crack distribution concentration, this study introduces the concept of entropy (Xu et al., 2020; Cheng et al., 2022; Han et al., 2023). The specific expression of entropy is provided in Eq. (8). The detailed calculation steps are as follows:

(1) Divide the specimen into 200 uniform grid units (10 × 20);
(2) Calculate the number of cracks in each grid unit;
(3) Determine the proportion of cracks in each grid unit relative to the total number of cracks in the specimen;
(4) Use Eq. (8) to calculate crack entropy.

A higher entropy value indicates a more disordered and uniform spatial distribution of cracks, while a lower entropy value indicates a more ordered and concentrated spatial distribution of cracks.

$$H = -\sum\nolimits_a \frac{n_a}{N_{\text{total}}} \log\left(\frac{n_a}{N_{\text{total}}}\right), \tag{8}$$

where H is the entropy; a is the number of uniformly divided grid units within the specimen; n_a is the number of cracks contained within the a-th grid unit; and N_{total} is the total number of cracks within the specimen.

The entropy values of cracks are shown in Fig. 11. As the strain rate increases from 6.25×10^{-5} to 6.25×10^{-3} s^{-1}, the crack entropy corresponding to σ_{ci}, σ_{cd}, and σ_p increases by 8.40%, 8.39%, and 3.60%, respectively. This indicates that the distribution of cracks becomes more uniform. From the perspective of the contribution of mineral crystal materials, at higher strain rates, more parts of rock materials play a supporting role, resulting in higher strength. This suggests that the greater the strain rate, the higher the strength exhibited by the material.

4.2 Stress distribution at the meso-scale

Based on the above-mentioned results, strain rate primarily influences the damage degree of various minerals

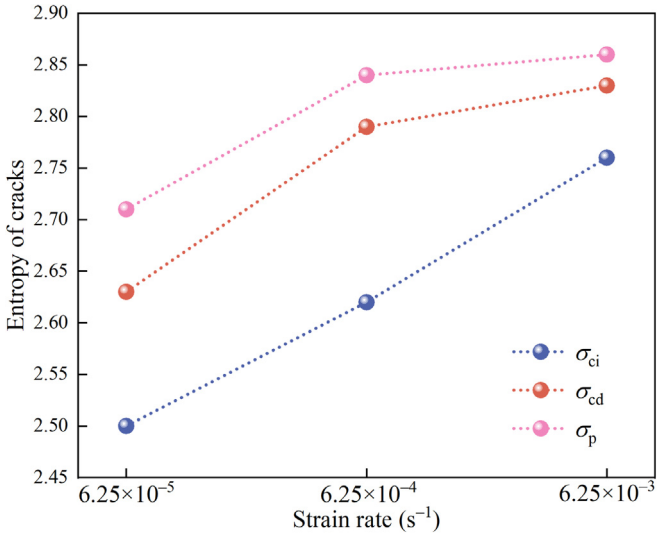

Fig. 11. Entropy of cracks.

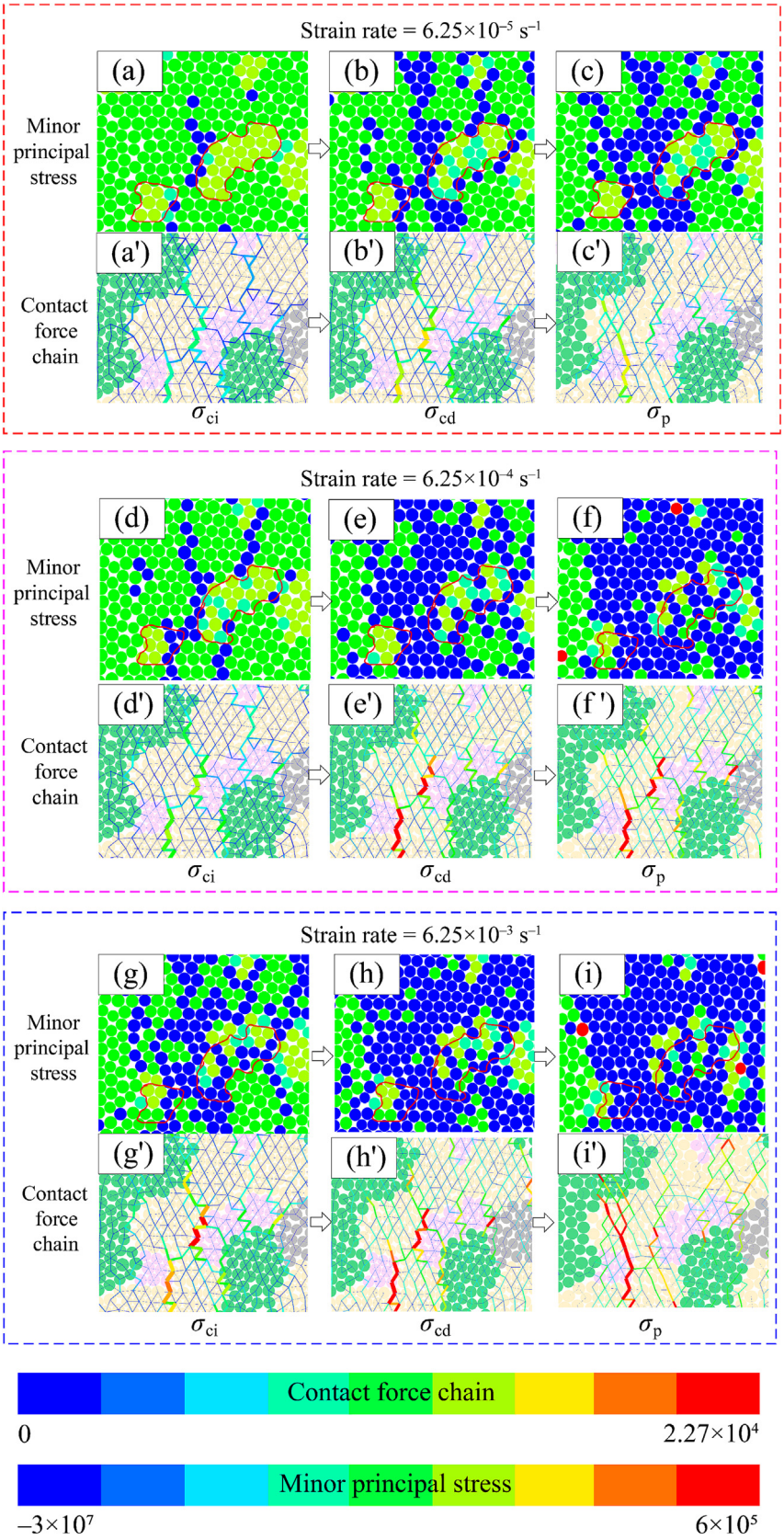

Fig. 12. Local damage maps of the GBM model at different strain rates. (a)–(i) represent the minor principal stress maps near biotite at different strain rates, and (a')–(i') represent the contact force chain maps near biotite at different strain rates.

in granite, with biotite exhibiting the most significant changes. This alters the controlling ability of biotite in crack propagation. To compare the strain rate effect on crack behavior in biotite, a detailed analysis of local damage near biotite, based on Fig. 10(a), (b), and (c), was conducted. The evolution of minor principal stress and contact force chains at different strain rates was obtained, as shown in Fig. 12, with the biotite regions outlined in red.

At a strain rate of 6.25×10^{-5} s^{-1}, granite exhibits a uniform stress distribution and contact force chain network at the crack initiation stage (Fig. 12(a) and (a')). As stress increases to the damage stage, concentration occurs in the biotite region, with contact force chains becoming more localized (Fig. 12(b) and (b')). At peak stress, stress is highly concentrated in the biotite area, and the contact force chain network begins to break, forming distinct cracks (Fig. 12(c) and (c')). Notably, at low strain rates, cracks tend to propagate around the biotite region, highlighting its significant role in guiding the crack path and causing cracks to follow the edges of biotite rather than propagate directly through it.

At a strain rate of 6.25×10^{-4} s^{-1}, the stress distribution and force chain concentration at the crack initiation stress stage slightly increase compared to the lower strain rate (Fig. 12(d) and (d')). At the damage stress stage, the concentration of stress and force chains in the biotite region becomes more pronounced, gradually forming stress concentration areas (Fig. 12(e) and (e')). At the peak stress stage, stress is highly concentrated in the biotite region, and the contact force chains exhibit significant rupture (Fig. 12(f) and (f')). At this point, the crack propagation path partially penetrates the biotite region. This suggests that at moderate strain rates (6.25×10^{-4} s^{-1}), cracks tend to both bypass and penetrate biotite, indicating a reduced but still present guiding effect of biotite on the crack path.

At a strain rate of 6.25×10^{-3} s^{-1}, the distribution of stress and contact force chains begins to concentrate at the crack initiation stress stage (Fig. 12(g) and (g')). However, upon entering the damage stress stage, the concentration in the biotite region intensifies significantly (Fig. 12(h) and (h')). At the peak stress stage, stress is highly concentrated in the biotite region, and the contact force chains completely break, representing brittle failure behavior (Fig. 12(i) and (i')). At high strain rates (6.25×10^{-3} s^{-1}), cracks tend to propagate directly through the biotite region. This suggests that under high strain rate conditions, the guiding effect of biotite on the crack path nearly disappears, and cracks are more likely to penetrate biotite directly, leading to rapid material failure and more intense crack propagation.

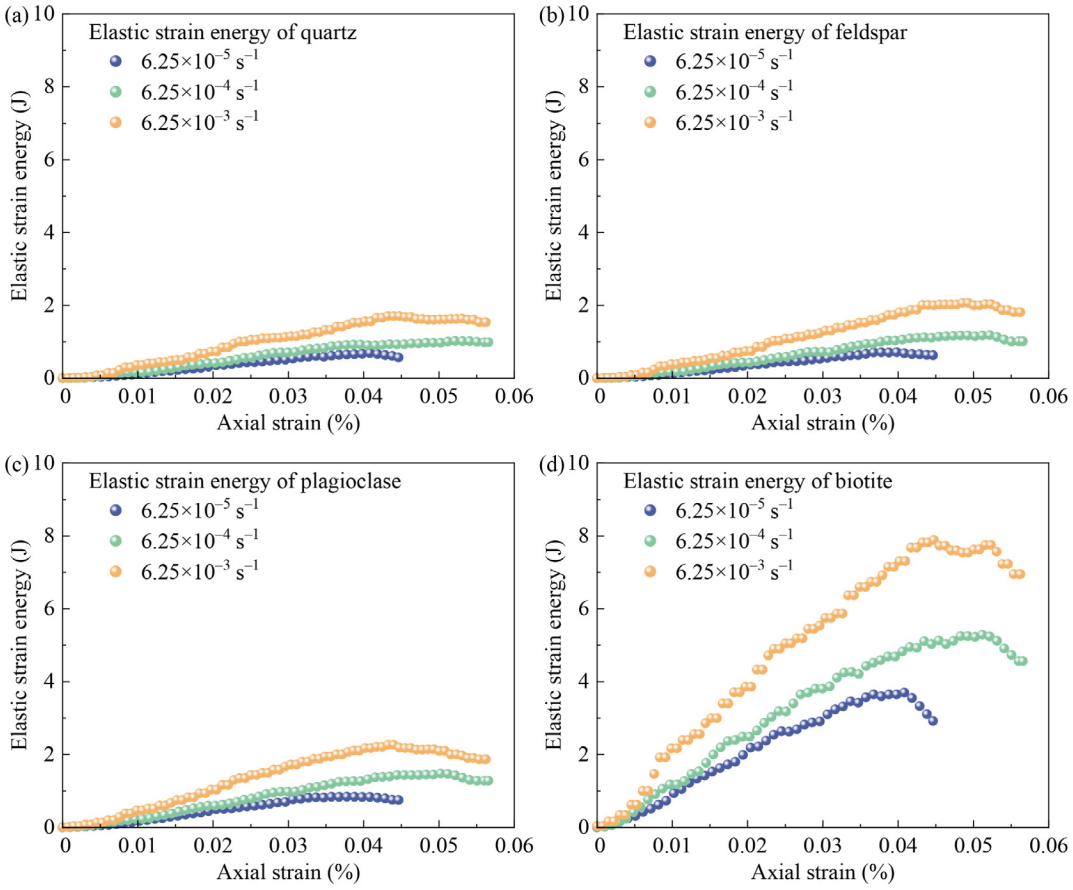

Fig. 13. Elastic strain energy of minerals at different strain rates. (a) Quartz, (b) feldspar, (c) plagioclase, and (d) biotite.

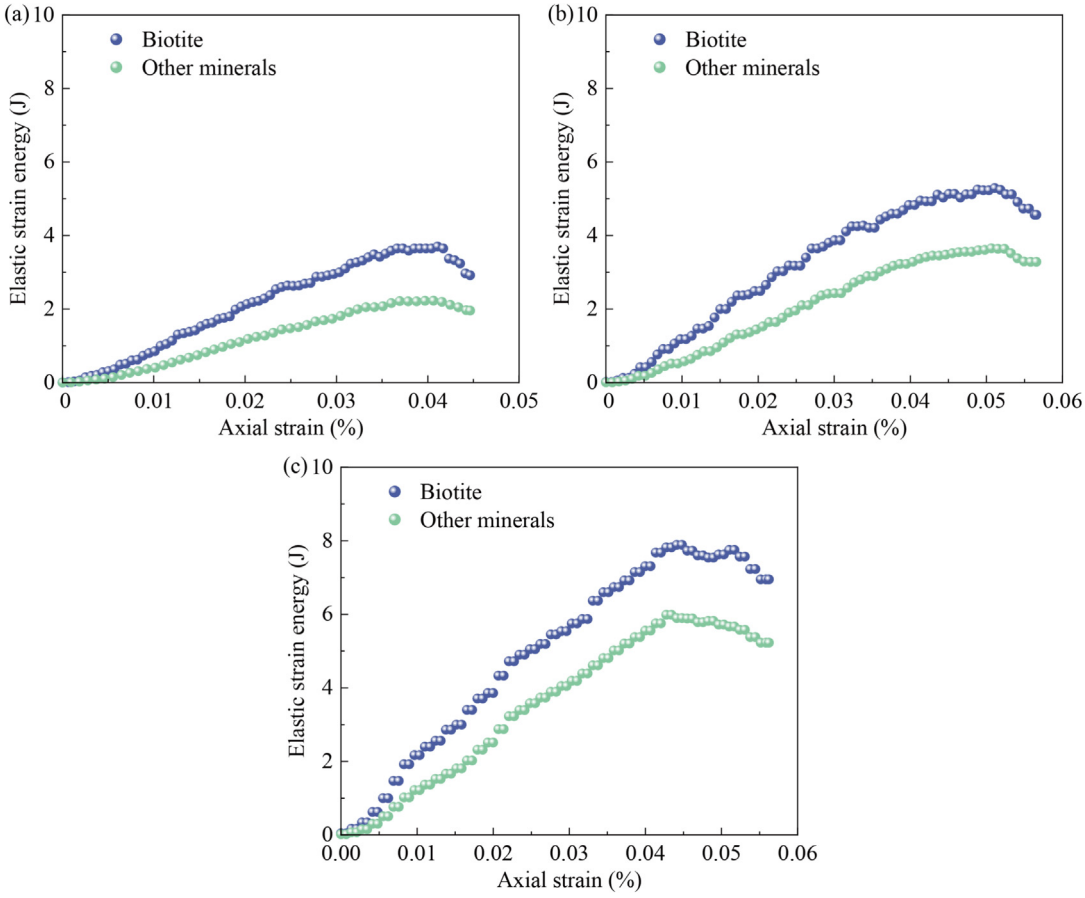

Fig. 14. Elastic strain energy of different minerals at the same strain rate. (a) Mineral elastic strain energy with a strain rate of 6.25×10^{-5} s^{-1}, (b) mineral elastic strain energy with a strain rate of 6.25×10^{-4} s^{-1}, and (c) mineral elastic strain energy with a strain rate of 6.25×10^{-3} s^{-1}.

4.3 Energy evolution at the meso-scale

The storage of elastic strain energy within minerals is closely linked to crack propagation behavior (Yin et al., 2021; Zhang et al., 2023). To further analyze the fracture mechanisms of soft minerals under different strain rates, the pre-peak elastic strain energy of various minerals was statistically calculated from an energy perspective, based on the principles described in Section 2.4. Figure 13 shows the changes in elastic strain energy for different minerals at various strain rates. As the strain rate increases, the elastic strain energy of each mineral gradually increases, with biotite exhibiting the highest elastic strain energy and quartz the lowest.

To better compare the elastic strain energy storage capacity of biotite with that of other minerals, Fig. 14 presents the changes in elastic strain energy with axial strain for biotite and other minerals (including quartz, feldspar, and plagioclase) at the same strain rate. The elastic strain energy increases with axial strain, and for all strain rates, biotite exhibits higher elastic strain energy than the other minerals. This suggests that biotite can accumulate more energy under the same strain conditions, demonstrating a higher elastic energy storage capacity (Zhang et al., 2023).

To quantitatively characterize the uniformity of elastic strain energy storage among minerals, the elastic strain energy of biotite and other minerals was normalized with respect to the total elastic strain energy using Eqs. (9)–(12).

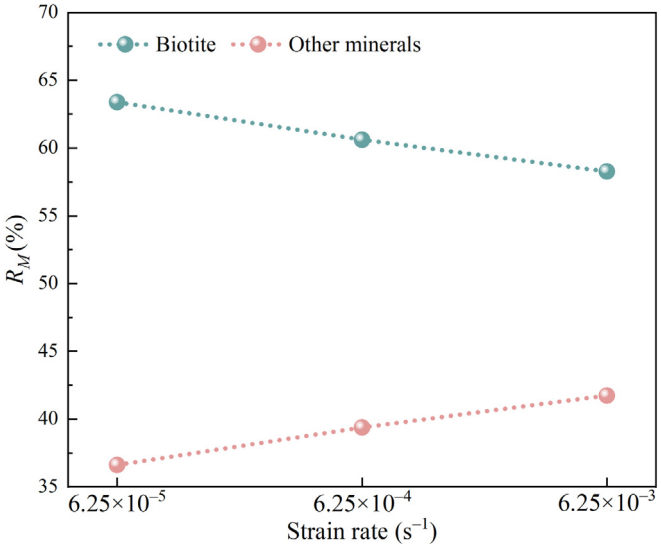

Fig. 15. Ratio of mineral elastic strain energy to total elastic strain energy at different strain rates.

$$\Delta U^{e} = \Delta U^{e\_Other} + \Delta U^{e\_Biotite}, \quad (9)$$

$$\Delta U^{e\_Other} = \Delta U^{e\_Quartz} + \Delta U^{e\_Feldspar} + \Delta U^{e\_Plagioclase}, \quad (10)$$

$$R_{M\_Biotite} = \frac{U^{e\_Biotite}}{\Delta U^{e}} \times 100\%, \quad (11)$$

$$R_{M\_Other} = \frac{U^{e\_Other}}{\Delta U^{e}} \times 100\%, \quad (12)$$

where ΔU^{e} represents the total elastic strain energy; $R_{M\_Biotite}$ represents the ratio of the elastic strain energy of biotite to the total elastic strain energy; and R_{M_Other} represents the ratio of the elastic strain energy of other minerals to the total elastic strain energy.

The resulting ratios of mineral elastic strain energy to total elastic strain energy at different strain rates are shown in Fig. 15. As the strain rate increases, $R_{M\_Biotite}$ gradually decreases from about 66% to 60%, indicating that the proportion of elastic strain energy stored in biotite decreases with increasing strain rate. Conversely, R_{M_Other} for other minerals gradually increases from 36% to about 40%, showing that the proportion of elastic strain energy stored in other minerals increases as the rate increases. This suggests that as the strain rate increases, the disparity in elastic strain energy among different minerals diminishes, leading to more uniform energy release and enhanced overall strength.

Based on the local damage around biotite (Fig. 12), the distribution of elastic strain energy in different minerals at various strain rates was statistically analyzed, as shown in Fig. 16. The white dotted regions indicate biotite, and the particle color represents the magnitude of elastic strain energy, ranging from blue (low elastic strain energy) to red (high elastic strain energy). As loading continues, the elastic strain energy stored in minerals increases. Compared with other minerals, biotite stores more elastic strain energy. At a low strain rate (6.25×10^{-5} s^{-1}), the high elastic strain energy of biotite imparts significant resistance to crack propagation. Cracks encountering biotite have insufficient energy to penetrate, causing them to bypass the biotite region (Fig. 10(d)). At a moderate strain rate (6.25×10^{-4} s^{-1}), the increased energy allows some cracks to overcome the resistance of biotite and begin to traverse the edges of the biotite region. At a high strain rate (6.25×10^{-3} s^{-1}), the elastic strain energy storage capacity of biotite becomes similar to that of other minerals, reducing the differences in elastic strain energy storage among

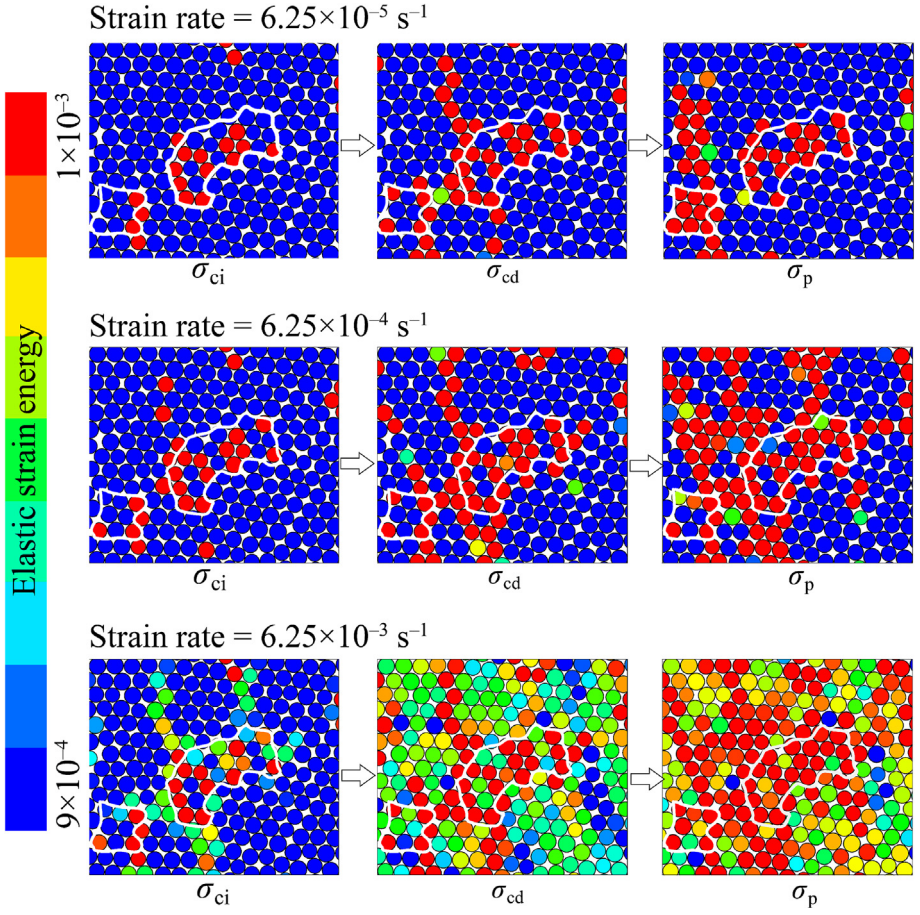

Fig. 16. Local distribution of elastic strain energy (Note: Blue indicates low elastic strain energy, red indicates high elastic strain energy, and the regions outlined by white lines indicate biotite minerals).

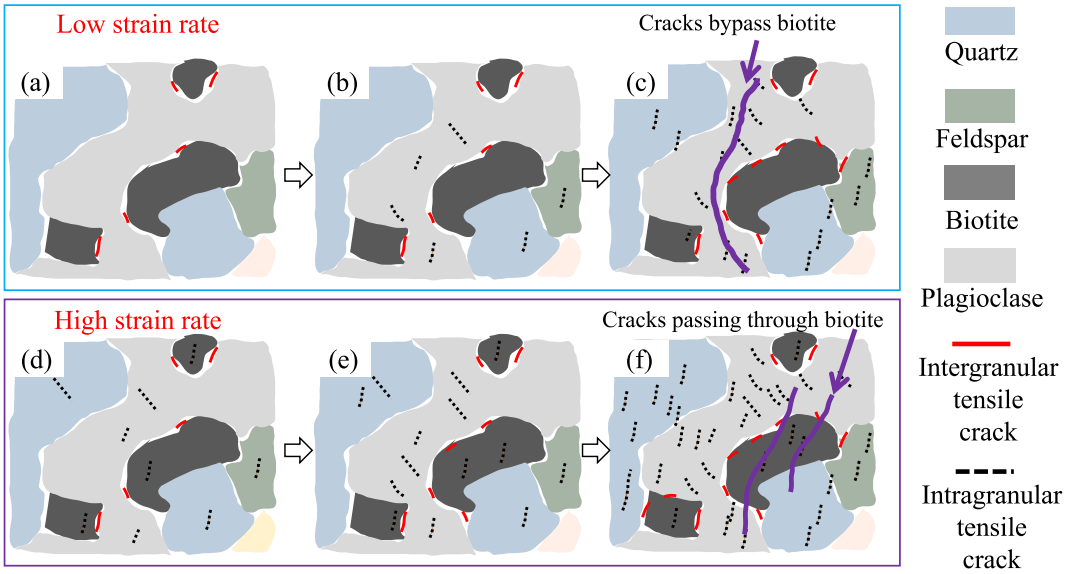

Fig. 17. Mechanism of crack propagation in biotite minerals at different strain rates.

minerals. This results in more uniform energy release and causes cracks associated with biotite to transition from intergranular to transgranular propagation.

4.4 Mechanism of strain rate effect on crack propagation

Under quasi-static loading conditions with low strain rates, there is sufficient time for stress redistribution, leading to stress concentration at the intergranular weak planes around biotite minerals, forming intergranular tensile cracks (Fig. 17(a)). As the load increases, cracks begin to propagate in plagioclase and potassium feldspar, generating intragranular tensile cracks (Fig. 17(b)) (Ghasemi et al., 2020). Biotite, with its lower stiffness and greater flexibility (Aboayanah et al., 2024; Ghasemi et al., 2024), has a higher capacity to store elastic strain energy, resulting in greater resistance to crack penetration. Consequently, cracks tend to propagate along the grain boundaries of biotite particles rather than directly through them (Fig. 17(c)).

Under high strain rate conditions, the initial loading results in high stress concentration within the biotite grains and between minerals, with insufficient time for stress redistribution. Consequently, cracks initiate both intergranular and intragranular tensile cracks along the biotite grains and within the minerals (Fig. 17(d)). As the load increases more dramatically, the fracture toughness of the material decreases (Li et al., 2020), leading to the formation of more intragranular tensile cracks within biotite (Fig. 17(e)). Under rapid loading conditions, the crack propagation rate increases significantly, and cracks do not have sufficient time to follow the energy-minimizing path around the biotite particles. Therefore, cracks tend to propagate along the shortest path, penetrating through biotite and rapidly releasing the accumulated energy (Fig. 17(f)).

Based on the results and discussion above, under unconfined loading conditions, rocks exhibit significant strain rate dependency at different strain rates. As the strain rate increases, the influence of soft minerals (i.e., biotite) on the rock fracture mode decreases due to differences in mineral properties. Therefore, in underground engineering excavation, when the excavation rate is low, soft minerals may play a significant role in absorbing strain energy, slowing the energy release process, and reducing the likelihood of rockburst hazards. However, at higher excavation rates, the influence of soft minerals on energy absorption diminishes, making the overall energy release process more intense and increasing the risk of rockburst. These insights are critical for guiding excavation strategies and enhancing the overall stability of underground spaces.

5 Conclusions

This study integrates MTI-LM and GBM techniques to investigate meso-scale crack propagation in granite under different strain rates. A crack entropy index was introduced to quantify crack concentration, and an energy-based analysis was conducted to reveal how strain rate influences the mechanical behavior and fracture mechanisms of rock. These findings have important implications for the stability and design of underground space engineering. The main conclusions are as follows:

(1) Effect on macroscopic mechanical parameters: The strength, elastic modulus, and axial strain of granite all increase with strain rate. The normalized crack initiation stress σ_{ci}/σ_p increases with strain rate, whereas the normalized crack damage stress σ_{cd}/σ_p decreases with strain rate.
(2) Crack propagation and failure mode: The crack entropy gradually increases, and the fracture mode related to biotite minerals transitions from intergranular to transgranular, indicating a more uniform distribution of microcracks.

(3) Strain rate effect mechanism: At low strain rates, microcracks preferentially propagate along intergranular paths, bypassing soft minerals to reduce energy consumption. In contrast, higher strain rates promote transgranular cracking along shorter paths, enhancing crack uniformity and energy dissipation, thereby improving the overall strength and stiffness of the rock.

Data availability

The data that support the findings of this study are available from the corresponding author upon reasonable request.

CRediT authorship contribution statement

Qinyuan Liang: Conceptualization, Writing – original draft, Formal analysis, Software, Investigation, Methodology. **Hengxing Lan:** Writing – review & editing, Funding acquisition, Project administration, Conceptualization, Supervision. **Yu Zhou:** Writing – review & editing, Validation, Methodology, Software, Conceptualization, Formal analysis. **Shijie Liu:** Methodology, Data curation, Writing – review & editing, Conceptualization. **Bo Li:** Writing – review & editing, Methodology, Software. **Langping Li:** Validation, Data curation, Conceptualization. **Han Bao:** Data curation, Conceptualization, Validation.

Declaration of competing interest

The authors declare that they have no known competing financial interests or personal relationships that could have appeared to influence the work reported in this paper.

Acknowledgement

The authors greatly acknowledge the financial support from the National Natural Science Foundation of China (Grant Nos. 42041006, 42402277, and 52204146), the Second Tibetan Plateau Scientific Expedition and Research (STEP) program (Grant No. 2019QZKK0904), and the Fundamental Research Funds for the Central Universities, CHD (Grant Nos. 300102265718 and 300102264902).

References

Aboayanah, K. R., Abdelaziz, A., Haile, B. F., Zhao, Q., & Grasselli, G. (2024). Evaluation of damage stress thresholds and mechanical properties of granite: New insights from digital image correlation and GB-FDEM. *Rock Mechanics and Rock Engineering*, *57*, 4679–4706.

Bao, H., Pei, R. S., Lan, H. X., Yan, C. G., Xu, J. B., Zhai, Y., & Xu, X. H. (2021). Damage evolution of Biotite quartz schist caused by mineral directional arrangement under cyclic loading and unloading. *Chinese Journal of Rock Mechanics and Engineering*, *40*(10), 2015–2026 (in Chinese).

Bao, H., Zhang, K. K., Yan, C. G., Lan, H. X., Wu, F. Q., & Zheng, H. (2020). Excavation damaged zone division and time-dependency deformation prediction: A case study of excavated rock mass at Xiaowan Hydropower Station. *Engineering Geology*, *272*, 105668.

Barber, C. B., Dobkin, D. P., & Huhdanpaa, H. (1996). The quickhull algorithm for convex hulls. *ACM Transactions on Mathematical Software*, *22*(4), 469–483.

Cheng, X., Tian, W., Gao, J. F., Guo, J., & Wang, X. H. (2022). Grey entropy analysis of strength and void structure of carbon nanotubes concrete under the coupling of sulfate attack and freeze-thaw cycles. *Construction and Building Materials*, *358*, 129462.

Cho, S. E. (2013). First-order reliability analysis of slope considering multiple failure modes. *Engineering Geology*, *154*, 98–105.

Doan, M. L., & Gary, G. (2009). Rock pulverization at high strain rate near the San Andreas fault. *Nature Geoscience*, *2*, 709–712.

Eberhardt, E., Stead, D., & Stimpson, B. (1999). Quantifying progressive pre-peak brittle fracture damage in rock during uniaxial compression. *International Journal of Rock Mechanics and Mining Sciences*, *36*(3), 361–380.

Feng, G., Wang, X. C., Kang, Y., & Zhang, Z. T. (2020). Effect of thermal cycling-dependent cracks on physical and mechanical properties of granite for enhanced geothermal system. *International Journal of Rock Mechanics and Mining Sciences*, *134*, 104476.

Feng, G., Zhu, C., Wang, X. C., & Tang, S. B. (2023). Thermal effects on prediction accuracy of dense granite mechanical behaviors using modified maximum tangential stress criterion. *Journal of Rock Mechanics and Geotechnical Engineering*, *15*(7), 1734–1748.

Gao, G., Yao, W., Xia, K., & Li, Z. (2015). Investigation of the rate dependence of fracture propagation in rocks using digital image correlation (DIC) method. *Engineering Fracture Mechanics*, *138*, 146–155.

Ghasemi, S., Khamehchiyan, M., Taheri, A., Nikudel, M. R., & Zalooli, A. (2020). Crack evolution in damage stress thresholds in different minerals of granite rock. *Rock Mechanics and Rock Engineering*, *53*, 1163–1178.

Ghasemi, S., Khamehchiyan, M., Taheri, A., Nikudel, M. R., Zalooli, A., & Sadeghi, E. (2024). The effect of cyclic loading parameters on the physical, mechanical, and microcracking behavior of granite. *Engineering Geology*, *332*, 107475.

Han, Z., Zhang, Y. S., Zhang, W. H., Qiao, H. X., Feng, Q., Xue, C. Z., & Shang, M. G. (2023). Study on comprehensive morphological parameters of manufactured sand based on CT scanning and entropy method and its application in rheology of manufactured sand mortar. *Construction and Building Materials*, *370*, 130628.

He, M. C., Cheng, T., Qiao, Y. F., & Li, H. R. (2023). A review of rockburst: Experiments, theories, and simulations. *Journal of Rock Mechanics and Geotechnical Engineering*, *15*(5), 1312–1353.

Huang, B. X., Li, L. H., Tan, Y. F., Hu, R. L., & Li, X. (2020). Investigating the Meso-mechanical anisotropy and fracture surface roughness of continental shale. *Journal of Geophysical Research: Solid Earth*, *125*(8), e2019JB017828.

Lambert, C., & Coll, C. (2014). Discrete modeling of rock joints with a smooth-joint contact model. *Journal of Rock Mechanics and Geotechnical Engineering*, *6*(1), 1–12.

Lan, H. X., Martin, C. D., & Andersson, J. C. (2013). Evolution of in situ rock mass damage induced by mechanical–thermal loading. *Rock Mechanics and Rock Engineering*, *46*, 153–168.

Lan, H. X., Martin, C. D., & Hu, B. (2010). Effect of heterogeneity of brittle rock on micromechanical extensile behavior during compression loading. *Journal of Geophysical Research: Solid Earth*, *115*(B1), B01202.

Li, B., Liang, Q. Y., Zhou, Y., Zhao, C., & Wu, F. Q. (2022). Research on crack propagation law of granite based on CT-GBM reconstruction method. *Chinese Journal of Rock Mechanics and Engineering*, *41*(6), 1114–1125 (in Chinese).

Li, X. F., Li, H. B., Liu, L. W., Liu, Y. Q., Ju, M. H., & Zhao, J. (2020). Investigating the crack initiation and propagation mechanism in brittle rocks using grain-based finite-discrete element method. *International Journal of Rock Mechanics and Mining Sciences*, *127*, 104219.

Li, X. F., Li, H. B., Zhang, G. K., Ju, M. H., & Zhao, J. (2021). Rate dependency mechanism of crystalline rocks induced by impacts: Insights from grain-scale fracturing and micro heterogeneity. *International Journal of Impact Engineering*, *155*, 103855.

Li, X. F., Zhang, Q. B., Li, H. B., & Zhao, J. (2018). Grain-based discrete element method (GB-DEM) modelling of multi-scale fracturing in rocks under dynamic loading. *Rock Mechanics and Rock Engineering*, *51*, 3785–3817.

Li, Y. R., Huang, D., & Li, X. A. (2014). Strain rate dependency of coarse crystal marble under uniaxial compression: Strength, deformation and strain energy. *Rock Mechanics and Rock Engineering*, *47*, 1153–1164.

Liang, C. Y., Wu, S. R., Li, X., & Xin, P. (2015). Effects of strain rate on fracture characteristics and mesoscopic failure mechanisms of granite. *International Journal of Rock Mechanics and Mining Sciences*, *76*, 146–154.

Liang, Q. Y., Lan, H. X., Zhou, Y., Li, B., Liu, S. J., & Bao, H. (2025a). Reverse size effect on unconfined compressive strength of red-bed rocks using micro-CT technique. *Journal of Rock Mechanics and Geotechnical Engineering*.

Liang, Q. Y., Lan, H. X., Zhou, Y., Li, B., Sun, W. F., Liu, S. J., & Lyu, W. J. (2025b). Reverse size effect of the unconfined compressive strength of crystalline rock: A grain-scale perspective. *Rock Mechanics and Rock Engineering*, *58*, 1651–1669.

Liang, Q. Y., Zhou, Z. H., Wang, Q., Jin, H. S., & Zhuang, S. Y. (2025c). Deciphering freeze–thaw induced degradation mechanisms in magnesium phosphate cement paste: Insights from three-dimensional quantitative characterization. *Cement and Concrete Composites*, 106283.

Liang, Q. Y., Zhao, C., Zhou, Y., Li, B., & Bao, R. Y. (2022). Investigation on the deformation and failure characteristics of shale samples containing circular hole considering the bedding angle effect under uniaxial compression. *Mathematical Problems in Engineering*, 2022, 1–10.

Liu, S. J., Lan, H. X., & Martin, C. D. (2022). Progressive transition from extension fracture to shear fracture of altered granite during uniaxial tensile tests. *Rock Mechanics and Rock Engineering*, *55*, 5355–5375.

Liu, S. J., Lan, H. X., Strom, A., Li, L. P., & Bao, H. (2024). Spatial segmentation of Jiali Fault's Holocene activity in the southeastern Tibetan Plateau. *NPJ Natural Hazards*, *1*, 42.

Martin, C. D. (1993). The strength of massive Lac du Bonnet granite around underground openings. [Doctoral dissertation, University of Manitoba, Canada].

Peng, J., Wong, L. N. Y., Teh, C. I., & Li, Z. H. (2018). Modeling microcracking behavior of Bukit Timah granite using grain-based model. *Rock Mechanics and Rock Engineering*, *51*, 135–154.

Potyondy, D. O., & Cundall, P. A. (2004). A bonded-particle model for rock. *International Journal of Rock Mechanics and Mining Sciences*, *41* (8), 1329–1364.

Rinehart, A. J., Bishop, J. E., & Dewers, T. (2015). Fracture propagation in Indiana Limestone interpreted via linear softening cohesive fracture model. *Journal of Geophysical Research: Solid Earth*, *120*(4), 2292–2308.

Saadat, M., & Taheri, A. (2019a). A numerical approach to investigate the effects of rock texture on the damage and crack propagation of a pre-cracked granite. *Computers and Geotechnics*, *111*, 89–111.

Saadat, M., & Taheri, A. (2019b). A cohesive discrete element based approach to characterizing the shear behavior of cohesive soil and clay-infilled rock joints. *Computers and Geotechnics*, *114*, 103109.

Tu, Y. L., Liu, X. R., Zhong, Z. L., & Li, Y. Y. (2016). New criteria for defining slope failure using the strength reduction method. *Engineering Geology*, *212*, 63–71.

Wang, H. L., Fan, P. X., Wang, M. Y., Li, W. P., & Qian, Y. H. (2011). Influence of strain rate on progressive failure process and characteristic stresses of red sandstone. *Rock and Soil Mechanics*, *32*(5), 1340–1346 (in Chinese).

Xiao, M. L., Xie, H. Q., Feng, G., He, Q., Liu, H. Z., & Zhuo, L. (2024). Investigation on the fracture mechanics characteristics and crack initiation of deep dense shale. *Engineering Fracture Mechanics*, *301*, 110039.

Xiao, Y. M., Qiao, Y. F., He, M. C., & Li, A. G. (2023). Strain rate effect of siltstone under triaxial compression and its interpretation from damage mechanics. *Rock Mechanics and Rock Engineering*, *56*, 8643–8656.

Xie, H. P., Li, L. Y., Peng, R. D., & Ju, Y. (2009). Energy analysis and criteria for structural failure of rocks. *Journal of Rock Mechanics and Geotechnical Engineering*, *1*(1), 11–20.

Xie, H. P., Zhu, J. B., Zhou, T., Zhang, K., & Zhou, C. T. (2020). Conceptualization and preliminary study of engineering disturbed rock dynamics. *Geomechanics and Geophysics for Geo-Energy and Geo-Resources*, *6*, 34.

Xu, Q., Wang, X. W., & Chen, J. J. (2020). Quantitative evaluation of pore-scale heterogeneity based on statistical analysis of a pore network model of unconsolidated porous media. *Hydrogeology Journal*, *28*, 1841–1852.

Xu, R. C., Zhang, S. Z., Li, Z., & Yan, X. M. (2023). Experimental investigation of the strain rate effect on crack initiation and crack damage thresholds of hard rock under quasi-static compression. *Acta Geotechnica*, *18*, 903–920.

Yin, X. M., Zhang, X., Lei, Y. J., & Wang, L. N. (2021). Effect of loading direction on the critical characteristic strength and energy evolution of quartz mica schist and microscale mechanisms. *Bulletin of Engineering Geology and the Environment*, *80*, 8693–8710.

Yu, H., Li, M., Pu, H., Zhang, L. Y., Chen, Y. L., Shi, X. Y., & Yue, Z. (2023). Direct tensile mechanical properties and damage fracture mechanisms of thermally damaged coal measures sandstone under high strain rate loading. *Journal of Materials Research and Technology*, *26*, 6356–6374.

Zhang, S. R., Xiao, W. F., & Jia, W. W. (2023). Modelling crack behavior of granite using multiscale grain-based model. *Simulation Modelling Practice and Theory*, *128*, 102813.

Zhao, K., Yu, X., Zhou, Y., Wang, Q., Wang, J. Q., & Hao, J. L. (2020). Energy evolution of brittle granite under different loading rates. *International Journal of Rock Mechanics and Mining Sciences*, *132*, 104392.

Zhou, L., Zhu, Z. M., Qiu, H., Zhang, X. S., & Lang, L. (2018). Study of the effect of loading rates on crack propagation velocity and rock fracture toughness using cracked tunnel specimens. *International Journal of Rock Mechanics and Mining Sciences*, *112*, 25–34.

Zhou, Y., Lyu, W. J., Li, B., Liang, Q. Y., & Wang, S. Q. (2025). A realistic 3D grain-based modeling approach for reproducing the mechanical and failure behavior of brittle granites. *International Journal of Rock Mechanics and Mining Sciences*, *185*, 105981.

Zhou, Y., Lyu, W. J., Li, B., & Liang, Q. Y. (2024a). Impact of soft minerals on crack propagation in crystalline rocks under uniaxial compression: A grain-based numerical investigation. *International Journal for Numerical and Analytical Methods in Geomechanics*, *48*(8), 2020–2042.

Zhou, Y., Lyu, W. J., Zhang, C., Zhou, Z. H., Wang, H. Y., Liang, Q. Y., Tang, Q. Q., Han, G. S., Guo, W., & Zhao, D. J. (2024b). Novel hard rock breaking technique using ultra-high-frequency particle impact induced by ultrasonic vibration field. *Energy*, *288*, 129747.

Zhou, Y., Lyu, W. J., Zhou, Z. H., Tang, Q. Q., Han, G. S., Hao, J. S., Chen, W. Q., & Wu, F. Q. (2023). New failure criterion for rock slopes with intermittent joints based on energy mutation. *Natural Hazards*, *118*, 407–425.

Zhu, J., Deng, J. H., Huang, Y. M., Liu, T., & Ma, Y. J. (2020). Study of loading rate effect on characteristic stresses of marble. *Journal of Harbin Institute of Technology*, *52*(2), 75–81 (in Chinese).